

The Multi-Instrument (EVE-*RHESSI*) DEM for Solar Flares, and Implications for Non-Thermal Emission

JAMES M. MCTIERNAN,¹ AMIR CASPI,² AND HARRY P. WARREN³

¹*Space Sciences Laboratory, University of California, Berkeley, CA 94720*

²*Southwest Research Institute, Boulder, CO 80302*

³*Space Science Division, Naval Research Laboratory, Washington, DC 20375*

ABSTRACT

Solar flare X-ray spectra are typically dominated by thermal bremsstrahlung emission in the soft X-ray ($\lesssim 10$ keV) energy range; for hard X-ray energies ($\gtrsim 30$ keV), emission is typically non-thermal from beams of electrons. The low-energy extent of non-thermal emission has only been loosely quantified. It has been difficult to obtain a lower limit for a possible non-thermal cutoff energy due to the significantly dominant thermal emission.

Here we use solar flare data from the EUV Variability Experiment (EVE) on-board the *Solar Dynamics Observatory* (SDO) and X-ray data from the *Reuven Ramaty High Energy Spectroscopic Imager* (RHESSI) to calculate the Differential Emission Measure (DEM). This improvement over the isothermal approximation and any single-instrument DEM helps to resolve ambiguities in the range where thermal and non-thermal emission overlap, and to provide constraints on the low-energy cutoff.

In the model, thermal emission is from a DEM that is parametrized as multiple gaussians in $\text{Log}(T)$. Non-thermal emission results from a photon spectrum obtained using a thick-target emission model. Spectra for both instruments are fit simultaneously in a self-consistent manner.

Our results have been obtained using a sample of 52 large (*GOES* X- and M-class) solar flares observed between February 2011 and February 2013. It turns out that it is often possible to determine low-energy cutoffs early (in the first two minutes) during large flares. Cutoff energies are typically low, less than 10 keV, with most values of the lower limits in the 5–7 keV range.

Keywords: Sun: corona — Sun: flares — Sun: UV radiation — Sun: X-rays, gamma rays

1. INTRODUCTION

Solar flare X-ray emission is commonly characterized as either “thermal” or “non-thermal.” In the standard flare model (e.g., [Shibata 1996](#)) the thermal component is “soft” X-ray emission due to bremsstrahlung radiation from a heated plasma, and the non-thermal component is “hard” X-ray emission due to bremsstrahlung from a beam of particles (usually assumed to be electrons) accelerated in a reconnection-related process in the solar corona. (See, for example, the review by [Benz 2017](#)).

The relative magnitudes and timing of the hard and soft components are illustrated in Figure 1, which shows X-ray emission observed by *RHESSI* (*Reuven Ramaty High Energy Solar Spectroscopic Imager*; [Lin et al. 2002](#)) and *GOES* (*Geostationary Operational Environmental Satellite*;

[Donnelly et al. 1977](#)) from a solar flare that occurred on 2011 February 15. The *RHESSI* light curves in the energy bands of 6–12 keV, 12–25 keV, 25–50 keV, and 50–100 keV show typical behavior; the lowest energy (thermal “soft” X-ray) emission is gradual, the highest energy (non-thermal “hard” X-ray) emission is impulsive, and the intermediate energy emission shows both characteristics. Flares typically exhibit the “Neupert Effect,” in which the derivative of the gradual soft X-ray time profile is similar to the time profile of impulsive hard X-rays ([Neupert 1968](#)).

Since the thermal and non-thermal emissions apparently overlap in energy, it has been a difficult problem to find a low-energy limit for the electrons responsible for the non-thermal emission, with estimates as low as 5–6 keV ([Kane et al. 1992](#)) to values as high as 50 keV or more ([Sui et al. 2007](#); [Warmuth et al. 2009](#)) and many values in between ([Aschwanden et al. 2016](#)). This value is important for determination of the energy released in non-thermal electrons; a difference of 10 keV in this parameter can result in

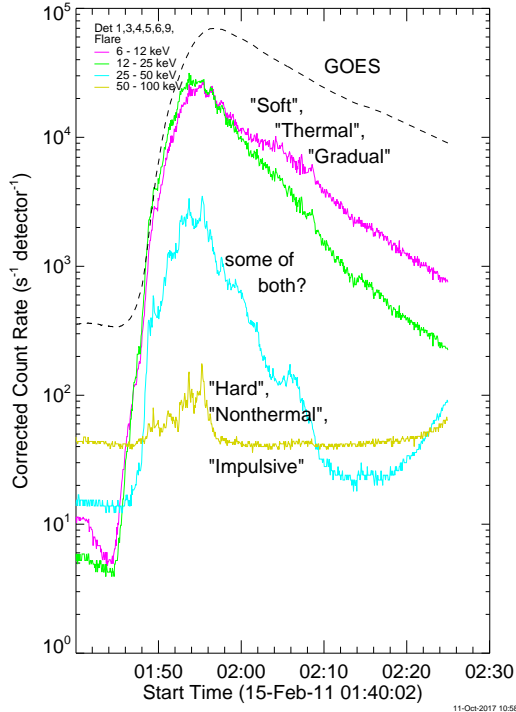


Figure 1. *RHESSI* and *GOES* light curves for an X-class flare on 2011 February 15. *RHESSI* curves (colors) are for the energy ranges of 6–12, 12–25, 25–50, and 50–100 keV. The *GOES* curve (dashed) is for the long wavelength (nominally 1–8 Å) channel.

orders of magnitude changes in the total energy required for the flare.

In this work, we combine *RHESSI* X-ray data with extreme ultraviolet (EUV) data from the EVE (EUV Variability Experiment; Woods et al. 2012) instrument on-board the *Solar Dynamics Observatory* (*SDO*; Pesnell et al. 2012) to calculate the Differential Emission Measure (DEM) for the thermal component of solar flares. This improvement over the isothermal approximation, and over DEMs derived from *RHESSI* alone, helps to resolve the ambiguity in the energy range where the thermal and non-thermal components may have similar photon fluxes, and hence where it is often difficult to differentiate between them using more naïve methods.

Previously we have shown that even though *RHESSI* and EVE are very different instruments, they can still be used in combination to self-consistently obtain the DEM in the ~ 2 –50 MK range (Caspi et al. 2014b). Because of the simultaneously complementary and overlapping temperature sensitivities of the two instruments, their joint DEM converges more stably, is more robust, and is significantly more accurate—particularly at the extreme ends of the temperature range—than when using one instrument in isolation. In that prior work, although we did fit the non-thermal component of the *RHESSI* spectra, we did not consider the resulting non-thermal parameters in any detail. In this work we are

interested in constraining low-energy cutoffs in the “residual” non-thermal spectrum, i.e., the *RHESSI* spectrum that is left over after the DEM has accounted for the bulk of the soft X-ray emission. Ideally, we would calculate the DEM using EVE alone, to independently assess the thermal X-ray emission which we would then subtract from *RHESSI* to obtain the residual, presumably entirely non-thermal, spectrum. However, this is not possible since the EVE DEM is not well-constrained at high ($\gtrsim 20$ MK) temperature (Warren et al. 2013) and the resulting predicted thermal X-ray component can therefore be grossly inaccurate (Caspi et al. 2014b). So, as in the prior work, we will fit the DEM plus non-thermal spectra simultaneously, with EVE and *RHESSI* together. We then use χ^2 values to determine limits for the low-energy energy cutoff in the non-thermal emission.

In the following section we discuss the DEM plus non-thermal model for the emission. This is followed by a description of the data set, then the results of the calculation, followed by discussion of the results.

2. DEM PLUS NON-THERMAL MODEL

The method we use for calculating the DEM has been presented in detail in Warren et al. (2013) and Caspi et al. (2014b); here we only give a brief overview. In the fitting model, the DEM is parametrized by a set of 11 Gaussian functions of $\text{Log}(T)$, equally spaced in the range of $\text{Log}(T)$ from 6.2 (~ 1.6 MK) to 7.8 (~ 63 MK). The width of each Gaussian is $d\text{Log}(T) = 0.02$, and is held fixed in the model. Only the Gaussian amplitudes vary. The amplitude of the 11th Gaussian (at ~ 63 MK) is held fixed to a small value, to increase the stability of the calculation, so the model DEM is effectively set to be zero at $\gtrsim 60$ MK. The original calculation (Caspi et al. 2014b) used 10 Gaussians and did not limit the amplitude for the highest temperature component; the limit imposed here improves fitting stability and is consistent with prior studies that found that flare plasma temperatures do not exceed $\gtrsim 50$ MK even for the largest recorded flares (Caspi et al. 2014a; Warmuth & Mann 2016). Following our previous work, we use coronal abundances for the demonstration of the DEM calculation, but we have also done the calculations including photospheric abundances and will discuss the effects of abundance variation, particularly for Fe.

The next step is to use the CHIANTI IDL package (Dere et al. 1997; Landi et al. 2013) to calculate the thermal EUV spectral irradiance from the DEM, for comparison with the EVE data. For *RHESSI*, the X-ray photon flux is calculated using `chianti_kev`, a database of pre-tabulated (for speed) CHIANTI-generated X-ray spectra, from the IDL SolarSoft (SSW; Freeland & Handy 1998) `xray` package, integrated over the instrument response to recover

a model *RHESSI* spectrum¹. Note that the original model discussed by Caspi et al. (2014b) separately fit Fe and Fe-Ni line complexes (at ~ 6.7 and ~ 8 keV). Here we use the line emission as calculated directly by the CHIANTI package.

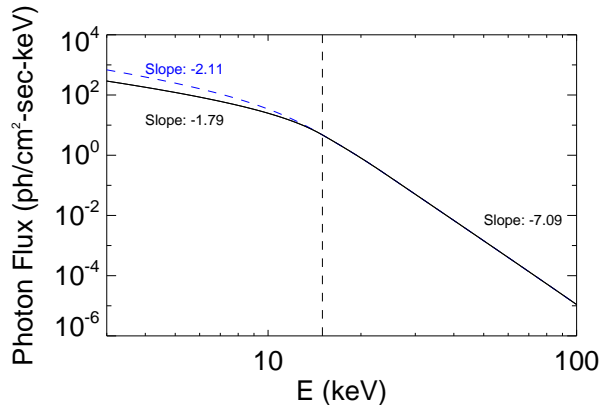


Figure 2. A sample thick-target X-ray photon spectrum, for $E_c = 15$ keV (dashed vertical line) and input electron spectral power-law index $\delta = -7.8$. Note that a sharp cutoff at E_c in the electron energy spectrum translates to a gradual rollover in the photon spectrum at energies below E_c . The blue dashed line below 10 keV shows the photon spectrum for a model with flat spectrum below E_c , see Sec. 6 for discussion.

To completely fit the *RHESSI* spectrum, a non-thermal emission model is necessary in addition to the thermal (DEM) component. We use the thick-target model (Brown 1971), as implemented by `f_thick2` in the `SSW xray` package. In this model, the non-thermal emission is assumed to be due to bremsstrahlung radiation from a beam of electrons, excited in the corona by an undetermined process, impacting the chromosphere and depositing all of their energy there. Although the electrons are beamed along magnetic field lines, the distribution of pitch angles (defined as the angle between the electron velocity vector and the local magnetic field) is assumed to be isotropic. This is a reasonable assumption for the relatively low electron energies in which we are interested (Leach & Petrosian 1981; McTiernan & Petrosian 1990). `f_thick2` uses the Haug (1997) approximation to the relativistic Bethe-Heitler bremsstrahlung cross-section (Eq. 3BN of Koch & Motz 1959). For an initial power-law electron beam with spectral index (negative log-log slope) δ and a low-energy cutoff at electron energy E_c , we expect to see a break (or, more correctly, a rollover) in the photon spectrum slightly below the electron cutoff energy, with the spectrum below E_c being flatter than the spectrum above, as shown in Figure 2. The photon spectral index below the cutoff has an asymptotic

value of ~ 1.8 , which is independent of the value above the cutoff. In Figure 2 the photon index γ above the cutoff is ~ 7.1 (for input electron $\delta = 7.8$).

In our model, using `f_thick2`, the electron distribution is parametrized as a broken power law, with both low- and high-energy cutoffs. The non-thermal parameters are: A_0 , the total integrated electron flux, in units of 10^{35} electrons s^{-1} ; A_1 , the power-law index of the electron distribution below a break energy E_{br} ; A_2 , the break energy E_{br} , in keV; A_3 , the power-law index above E_{br} ; A_4 , the low-energy cutoff E_c , in keV; and A_5 , the high-energy cutoff, in keV. Including the 11 parameters for the DEM and these 6 for the non-thermal model, there are 17 total model parameters.

The spectral fit procedure minimizes $\chi^2 = \chi_{RHESSI}^2 + \chi_{EVE}^2$, which for each instrument is defined as

$$\chi^2 = \sum_i (f_{i,model} - f_{i,obs})^2 / \sigma_i^2, \quad (1)$$

where $f_{i,model}$ is the model data (spectral irradiance for EVE, photon count rate for *RHESSI*), $f_{i,obs}$ is the observed data, and σ_i is the measurement uncertainty. For *RHESSI*, the uncertainty in each energy channel is estimated using Poisson statistics: $\sigma_{i,RHESSI} = \sqrt{f_{i,obs} / \delta t}$, where δt is the time interval duration. For EVE, the uncertainty is given by the observed standard deviation (from calibrated Level 2 EVE data) of the individual irradiance measurements during the time interval, divided by the square root of the number of 10 s spectra averaged for the time interval (Warren et al. 2013).

For EVE, a pre-flare background spectrum is subtracted to isolate the flare emission; this is obtained for a three-minute interval immediately before the associated *GOES* flare. For *RHESSI* the process is more complicated, because the background level depends on spacecraft position; it increases at high spacecraft latitude. The background levels shown in McTiernan (2009), valid for the 2002–2006 period, have the appropriate latitude variation but are not applicable for the time intervals used here due to long-term detector changes that result in higher background levels later in the mission. Here, for a given flare, we use the background spectrum during the nearest low-latitude spacecraft night interval, accounting for the long-term increase in background values. The spectrum is then further modified for latitude variations using the results presented by McTiernan (2009).

Figure 3 is a diagnostic plot that we use to check the goodness of fit for the full process. The upper left corner shows the (recovered) model DEM. The upper right shows a comparison plot of the *RHESSI* count spectrum, with black denoting the observed data and red the data expected from the model. Just below we show a plot of the residuals for the *RHESSI* portion of the fit (normalized by the uncertainty in each energy channel). The lower panel shows a comparison of the EVE spectrum, with observed data in black, and model data

¹ See <https://hesperia.gsfc.nasa.gov/rhessidatcenter/software/installation.html>

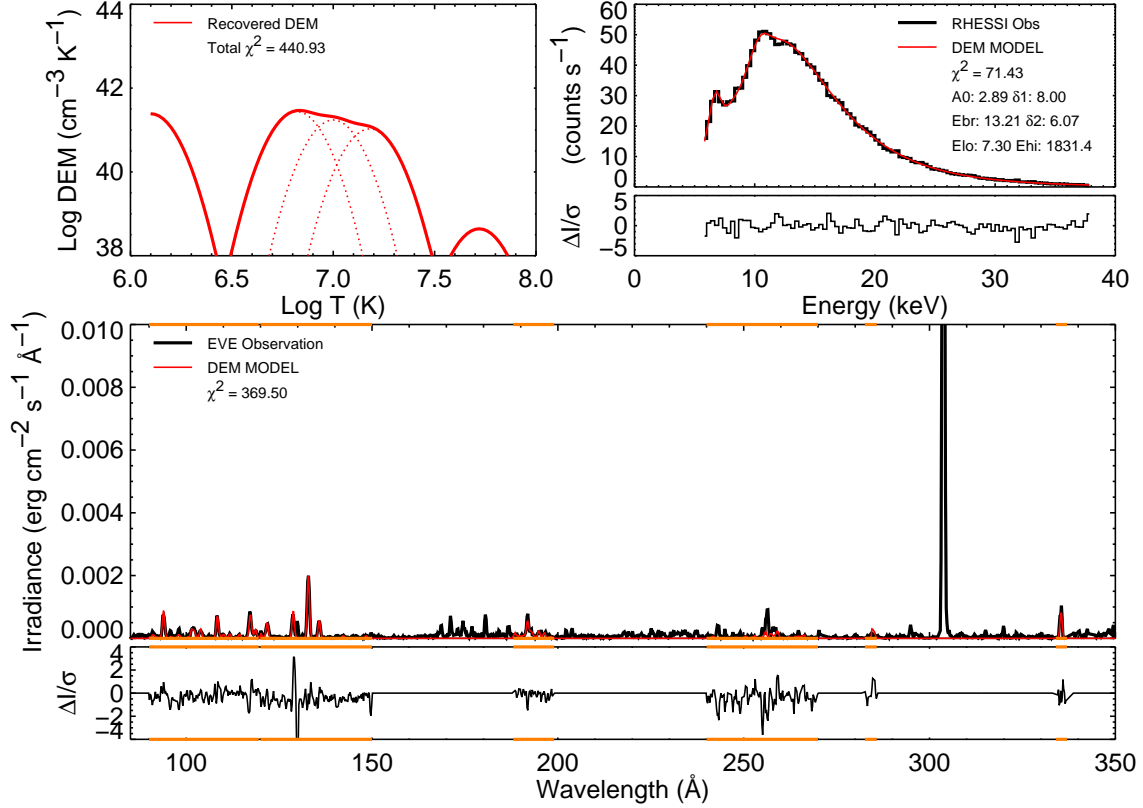


Figure 3. Diagnostic plot showing the goodness of fit early in the M7 flare of 2011 February 13 at 17:32:36 UT. Upper left: Log(DEM). Upper right: *RHESSI* count rate spectrum and residuals. Lower: EVE spectrum and residuals. Orange wavelength ranges in the EVE plots include prominent flare lines and are used for fitting; non-orange ranges are ignored.

in red. Note that not all of the EVE spectrum is used for fitting; we only consider wavelength bands that include prominent spectral lines associated with flares (these are, mostly, relatively high-temperature Fe lines; see Warren et al. 2013 for more details), highlighted in orange. The residual values for the EVE spectrum are shown in the bottom-most panel.

There are many more data points used in each EVE spectrum (~ 400) than there are in the typical *RHESSI* spectrum (~ 100), so we have changed the weighting of the EVE data in the fits by assuming a lower limit to the value of the EVE uncertainties, $\sigma_{i,EVE} \geq 0.04 \times f_{i,EVE}$. This is done to ensure that *RHESSI* data points are not ignored during the fit process; Figure 4 shows a comparison of spectra for the limited (weighted) versus unlimited fit. As is shown in the bottom panel, without these limits to the EVE uncertainties, the *RHESSI* spectrum is effectively ignored in the full process.

3. DATA SET

From Figure 1, we can see that the relative amount of thermal to non-thermal emission increases over time during an event. When the non-thermal component is only a small fraction of the total emission, it becomes difficult to constrain the low-energy cutoff E_c through spectral fitting. Thus, we

would like to perform this calculation as early during a flare as possible.

Figure 5 shows a *RHESSI* spectrum early during a flare when the thermal component is not overwhelmingly large. As a first cut, the spectrum has been fit using two isothermal components (red, blue) and a non-thermal component (green). Even in the $\lesssim 10$ keV range, the photon flux from the non-thermal component is not much smaller than that for thermal emission; this makes this time interval a good candidate for possibly isolating a cutoff energy. Conversely, Figure 6 shows a spectrum for a later time interval when the thermal component is much more prominent. Here, the “crossover” energy, where the thermal and non-thermal emissions are approximately the same, is ~ 30 keV. Below this crossover energy, the non-thermal contribution to the total model becomes vanishingly small ($< 1\%$ for energies $\lesssim 15$ keV), and it is clear that a spectral rollover corresponding to an electron cutoff E_c can “hide” nearly anywhere under the dominant thermal emission below the crossover energy. Thus, E_c would be constrained only as a relatively high upper limit, and this kind of spectrum is not a good candidate for finding E_c . For this reason, we restrict our analysis to the first two minutes of the flares in our sample.

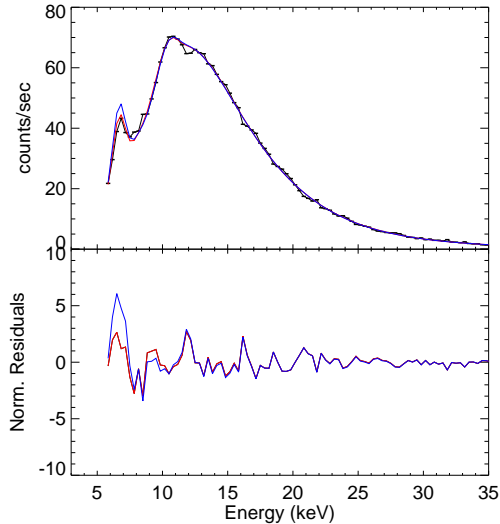


Figure 4. Comparison of *RHESSI* spectral fits for the same time range as Figure 3 (2011 February 13 17:32:36 UT). Top: black horizontal lines – observed count rate spectrum; red line – model results for “weighted” fit (i.e., where EVE uncertainties are increased so *RHESSI* data more strongly influences the fit process); blue line – model results for “unweighted” fit. Bottom: fit residuals for both cases; the unweighted model clearly yields a poorer fit to the *RHESSI* data at lower energies (where thermal emission dominates).

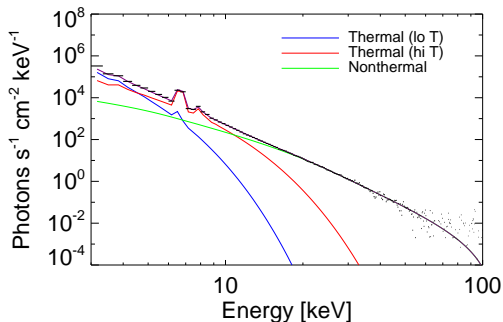


Figure 5. *RHESSI* photon spectrum for 2011 February 13 17:32:36 UT, fit with two isothermal components (red, blue) and a non-thermal component (green). Early in the flare, the ratio of non-thermal to thermal emission is high, making it easier to estimate the low-energy cutoff of the non-thermal electron distribution.

For this study, we work with a sample of 52 flares observed by both EVE and *RHESSI* during the period from February 2011 to February 2013. Each flare is of *GOES* class M or larger and has X-ray emission observed by *RHESSI* at energies above 50 keV. From each flare, we isolated one or two time intervals of approximately one minute duration with good conditions, i.e., occurring during the first two minutes of the “impulsive” emission >25 keV, with a discernible non-thermal component, with a relatively flat high-energy spectrum (thick-target electron spectral index $\delta < 10$), and with a

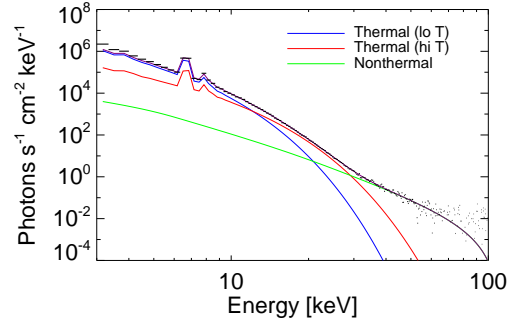


Figure 6. *RHESSI* spectrum for 2011 February 13 17:35:08 UT, again fit with two isothermal components (red, blue) and a non-thermal component (green). At later times in an event, the thermal emission dominates over the non-thermal at lower energies, making the low-energy cutoff difficult to estimate except as an upper limit.

good signal-to-noise ratio up to at least 50 keV. From these 52 flares, we found 66 appropriate time intervals for which we could perform the DEM calculation as described above. To establish limits on the low cutoff energy, for each time interval we iteratively fit the DEM plus f_{thick2} model for fixed values of the cutoff E_c ranging from 5 to 30 keV. We then examined curves of the goodness of fit parameter, χ^2 , to establish lower and upper limits on E_c .

4. RESULTS FOR A SINGLE TIME INTERVAL

Figure 7 shows the χ^2_{RHESSI} from the DEM+non-thermal fits plotted as a function of the cutoff energy E_c , for the 2011 February 13 flare. For this time, early in the flare, we have a pretty good result, and it is easy to identify upper and lower limits for the cutoff energy. This χ^2 curve shape was typical for most of the intervals analyzed, where the lower limit is generally 5 to 7 keV and the upper limit is usually in the 8–10 keV range. These limits are determined by identifying the E_c values where χ^2_{RHESSI} is less than 6.63 above its minimum value, which corresponds to the 99% confidence limit for the χ^2 distribution (Press et al. 1992).

It is instructive to examine the residuals of the spectral fits to better understand why a “bad” fit is bad, beyond just looking at χ^2 values. Figure 8 compares the *RHESSI* count spectra for the best fit E_c value of 7 keV (red), with a poorly-fit value of 16 keV (blue). For the too-high cutoff, the model spectrum does not fit the data well in the energy range of 10–20 keV well. Since the high cutoff value restricts how much non-thermal emission can be included in this energy range, the fit procedure tries to replace this with thermal emission. This, in turn, results in too many counts in the ~ 6.7 keV Fe line complex which is very sensitive to high temperatures. In this manner, the amount of emission seen by *RHESSI* in the Fe line limits the allowable amount of high- T emission measure. The requirement of fitting the EVE spectrum lim-

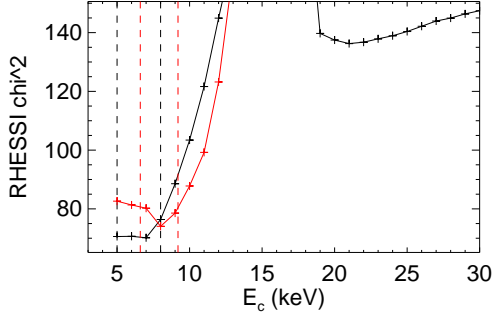


Figure 7. χ^2_{RHESSI} vs. low cutoff energy E_c for the time interval in Figure 5, using coronal (black) and photospheric (red) abundances. Dashed lines denote upper and lower limits for E_c , defined as the points on the curve where $\chi^2(E_c)$ passes through $\min(\chi^2) + 6.63$, corresponding to the 99% confidence limit for the χ^2 distribution.

its the amount of low- T emission measure. Thus, there must be a substantial amount of non-thermal emission in the 10–20 keV range, and this brackets the allowable E_c values.

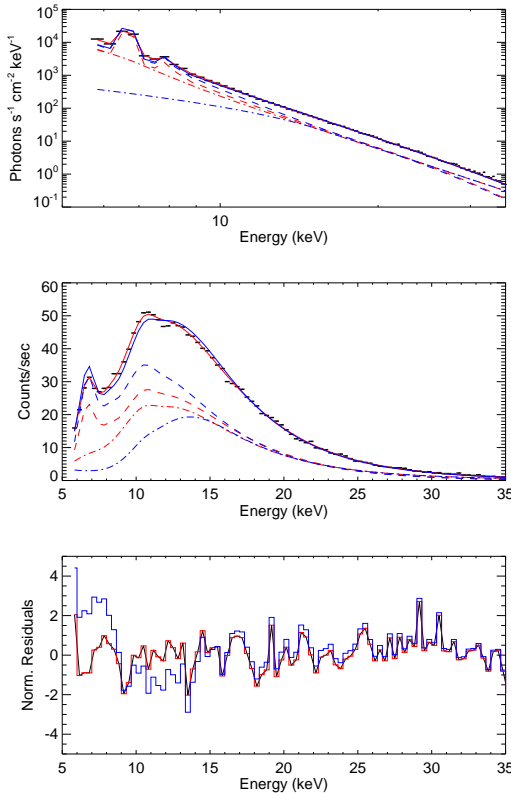


Figure 8. Top: *RHESSI* photon spectra (black) for 2011 February 13, 17:32:36 UT, with two model fits: best-fit model with E_c of 7 keV (red), and 16 keV (blue). Dash and dash-dot lines for each color denote the thermal and non-thermal contributions, respectively. Middle: count-rate spectra corresponding to above. Bottom: normalized residuals for the two spectral models.

Since the analysis depends on observed counts in the Fe line complex, it is possible for results to be affected by abundance variations. Although analysis of EVE flare spectra has suggested a nearly photospheric composition for most studied events (Warren 2014), analysis of other data has yielded different results (e.g., Dennis et al. 2015; Doschek & Warren 2017), and the issue is not yet resolved. In Figure 7, the red lines show the χ^2_{RHESSI} curve and E_c limits that result if we do the calculation using photospheric abundances, where the Fe abundance is approximately 4 times smaller than in the coronal case; the E_c limits derived this way are somewhat higher. Although for this time interval the minimum χ^2_{RHESSI} value using coronal abundances is smaller—by ~ 3 —than that for photospheric abundances, this difference is not large enough to rule out the photospheric case solely based on χ^2 . In future work we will include elemental abundances as fit parameters which can vary during processing.

5. RESULTS FOR THE FULL SAMPLE

Table 1 is a comparison of the cutoff values and limits from the EVE-*RHESSI* DEM models. The table columns show: interval date and time; derived limits for E_c and for \mathcal{E}_t (the total integrated electron energy flux) using coronal and photospheric abundances; the difference between \mathcal{E}_t and the value of \mathcal{E}_t for $E_c = 15$ keV; values of reduced χ^2_{RHESSI} for coronal and photospheric abundances (all of which are reasonably small); the ratio $R(Fe)$ of the *RHESSI* count rate in the ~ 6.7 keV Fe line complex to the peak of the count rate in the 10–12 keV range (see the middle panel of Figure 8, that shows the two peak structure in the *RHESSI* count spectrum); and the ratio $R_f(Fe)$ of the photon fluxes in these same energy ranges. A value of “NA” for $R(Fe)$ means that there was no separate peak in the count spectrum (because the thin attenuator was not engaged at that time), and we are unable to calculate that ratio.

In the initial step of the process, we use *RHESSI* data along with the SolarSoft *OSPEX* package² to initialize the detector response matrix, observed and background count rates, and initial parameters for the non-thermal spectra. This procedure models the thermal emission using two isothermal components as in Caspi & Lin (2010). This means that we can, in principle, compare the *RHESSI*-EVE results directly with *RHESSI* alone. It turns out that, for 30 of the 66 intervals, the value of E_c returned by a *RHESSI*-only calculation are within the limits obtained with *RHESSI* and EVE. The uncertainties returned by the *OSPEX* procedure, however, are quite large; for 36 of the intervals, the returned uncertainty is NaN. Only 7 intervals return an uncertainty of less than 10 keV. We believe that this justifies the use of the joint *RHESSI*-EVE procedure.

² See <https://hesperia.gsfc.nasa.gov/ssw/packages/spex/doc/>

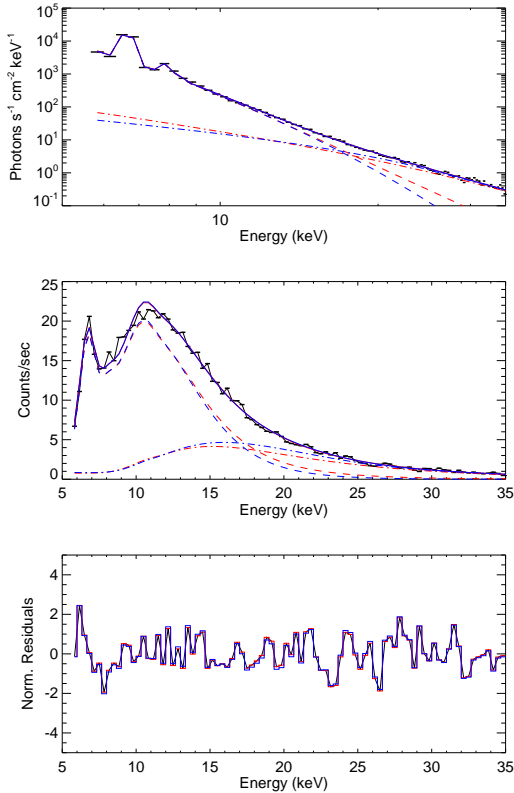


Figure 9. Top: *RHESSI* photon spectra for 2011 February 16, 14:23:04 UT, highlighting the effect of a relatively high Fe line-to-continuum ratio. Black – observed flux; red – best-fit model with $E_c = 7$ keV; blue – model with $E_c = 25$ keV. Dash and dash-dot lines for each color denote the thermal and non-thermal contributions, respectively. Middle: count-rate spectra corresponding to above. Bottom: normalized residuals for the two spectral models. Despite the significant difference in E_c , the two model photon spectra are nearly identical.

For most of the examined intervals we managed to get limiting values for E_c even when fits to *RHESSI* data alone (without EVE) returned *NaN* or very large uncertainties. For 16 of the 66 intervals, the χ^2 curve using coronal abundances was flat or bi-modal, so there are 50 good sets of derived limits. Using photospheric abundances, there are 57 good sets of limits.

The 16 time intervals for which we obtained no good E_c limits with coronal abundances can be divided into three different categories. (1) Nine are characterized by high Fe line emission relative to the peak emission in the 10–12 keV range ($R(Fe) \gtrsim 1$), as shown in Figure 9 and in Table 1. These tend to have very flat spectra below the break energy E_{br} and above the cutoff value E_c , and the resulting photon spectra for low and high E_c values are similar. (2) Three are bi-modal in χ^2 , and for low E_c values the best-fit non-thermal component has a very steep upward break around ~ 15 keV that offsets the higher- T emission measure needed for high E_c , as shown

in Figure 10. (3) For the remaining times, there is no obvious pattern in the spectra or fitting behavior to indicate why we cannot obtain a limit from the χ^2 curve.

Note that the values of χ^2_{RHESSI} are lower for coronal abundances, compared to photospheric, for 36 of the intervals.

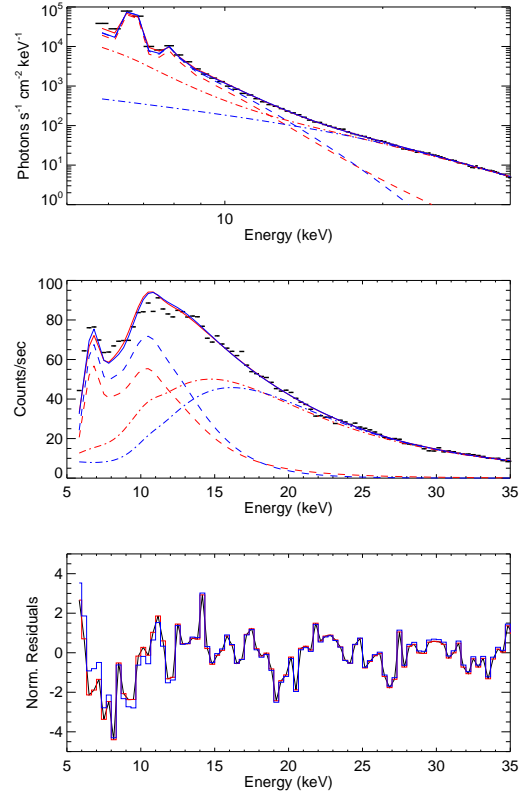


Figure 10. Top: *RHESSI* photon spectra for 2011 July 30, 02:07:32 UT, where for low E_c values a very steep upward break in the non-thermal component around ~ 15 keV offsets the higher- T emission measure needed for high E_c . Black – observed flux; red – best-fit model with $E_c = 7$ keV; blue – model with $E_c = 21$ keV. Dash and dash-dot lines for each color denote the thermal and non-thermal contributions, respectively. Middle: count-rate spectra corresponding to above. Bottom: normalized residuals for the two spectral models. Despite the significant differences in the thermal and non-thermal contributions for the two values of E_c , the total spectra for the two cases are similar.

Figure 11 shows histograms of derived cutoff energies. Most of the E_c are less than 10 keV (40 of 50 for coronal abundances, 47 of 57 for photospheric). Many intervals (33 coronal, 28 photospheric) have lower E_c limits of 5 keV, in the range where *RHESSI* begins to lose sensitivity (Smith et al. 2002). For those cases the lower limit may be less than 5 keV since we do not include *RHESSI* data below 5 keV in processing. A similar number (31 coronal, 25 photospheric) have both upper and lower limits at or below

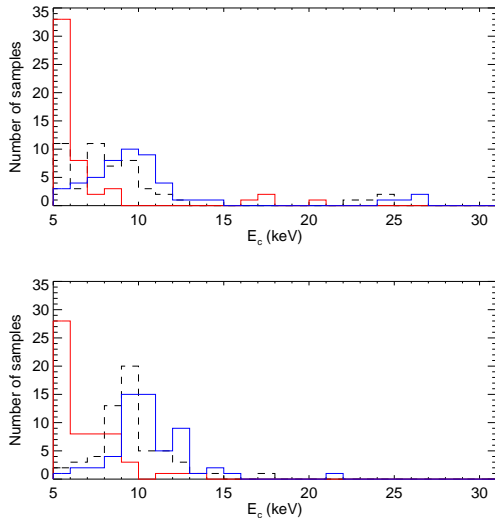


Figure 11. Top: Histograms of best-fit (black), and lower (red) and upper (blue) limits, for the low-energy cutoff E_c for the 50 time intervals with discernible limits using coronal abundances. Bottom: as above, for the 57 time intervals with good limits using photospheric abundances.

10 keV. Only a few intervals (4 coronal, 3 photospheric) have lower E_c limits above 10 keV.

6. DISCUSSION AND CONCLUSIONS

We have shown that the *RHESSI*-EVE DEM model often gives values for upper and (sometimes) lower limits to the non-thermal low cutoff energy E_c , early in flares when the thermal emission does not overwhelm the non-thermal component. These derived cutoff energies are typically low, below 10 keV, with most values of the lower limits in the 5–7 keV range and upper limits below 20 keV. These results are for coronal abundances; for photospheric abundances, the E_c values are typically slightly higher. For most of the analyzed time intervals, upper limits for E_c can be obtained because the amount of high- T emission measure is limited by the flux observed in the ~ 6.7 keV Fe line complex. For time intervals with a relatively large amount of Fe line emission, however, roughly 1/6th of the sample, this constraint is not available and we do not obtain good limits for E_c . Note that the “high-Fe” flares exhibit significant high- T components at the start of the hard X-ray emission, and thus do not fit in well with the standard flare model interpretation of thermal plasma being the result of “chromospheric evaporation” driven by energy deposition from non-thermal electrons. These may be examples of *in-situ* heating as discussed by, e.g., Caspi & Lin (2010), Longcope & Guidoni (2011), and Caspi et al. (2015a).

We chose the thick-target model with a sharp cutoff for this work for convenience and because it is well defined and well known in the community. We obtain similar results us-

ing more realistic thick-target electron models which have a flat electron spectrum below E_c (e.g., Saint-Hilaire & Benz 2005). We have reprocessed the sample times, using a model with a flat spectrum below E_c , and find a 1 to 2 keV difference between limits obtained using the flat cutoff model and the sharp cutoff model for most flares, and particularly for the flares with low E_c values. This is because the photon spectra for the two different models do not differ very much in the few keV just below E_c . This can be seen in Figure 2, where we compare the spectra for the sharp and flat cutoff cases. Since the low-cutoff flares have upper limits from 7 to 10 keV, and the models are only fit above 5 keV, we should not expect to see much difference. For example, in Figure 12, we compare the χ^2 curve for a sharp cutoff to the flat cutoff curve, and the difference in the upper limit found is 1 keV. For the full sample, the difference between E_c for the flat cutoff and E_c for the sharp cutoff is less than 2 keV for 59 of 66 intervals.

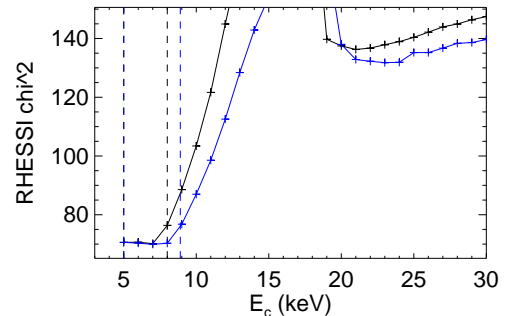


Figure 12. χ^2_{RHESSI} vs. low cutoff energy E_c for the time interval in Figure 5, for a sharp (black) and flat (blue) cutoffs. Dashed lines denote upper and lower limits for E_c . The flat cutoff model has an upper limit for E_c about 1 keV greater than the sharp cutoff model.

We have also tested thin-target electron models and *ad hoc* (empirical) sharply-broken power-law photon spectra with photon spectral index below a given E_c fixed at 1.5 versus the ~ 1.8 and ~ 2.1 gradual rollovers seen from the *f_thick2* models shown in Figure 2. We obtain similar results for this model as for thick and thin-target models.

The main conclusion to take away from this work is that, for most of the flares in the sample, it is possible to obtain limits on E_c early in the flare. Values are relatively low (< 10 keV) because the amount of emission observed in the ~ 6.7 keV Fe line complex limits the amount of high- T emission measure, and therefore limits the thermal continuum contribution to the energy range above 10 keV. These results are not very dependent on the details of the non-thermal model and should be valid for *any* model with a cutoff in the electron distribution, or that requires a relatively flat photon spectrum below an energy E_c .

Ours are lower limits than have been determined in past calculations using *RHESSI* data, such as Sui et al. (2007) or Saint-Hilaire & Benz (2005), which are typically above 15 keV. It has been pointed out that relatively low values of E_c often imply very large values for the non-thermal electron flux needed to account for the observed emission, i.e., the so-called “number problem” (Benz 2017). This remains true here: in the sixth column of Table 1, we show $\text{Log}(\mathcal{E}_{diff})$, the difference between the amount of total electron energy flux \mathcal{E}_t required for the best-fit value of E_c , and the amount of energy flux for $E_c = 15$ keV. For 42 of the 66 samples, this value is greater than 1.0 (i.e., we require more than an order of magnitude more electron energy than for the 15 keV cutoff).

Even more realistic non-thermal models including, for example, return current or “warm-target” plasma (Zharkova et al. 1995; Kontar et al. 2015), may perhaps help to mitigate this “number problem.” Many of our lower E_c limits of 5–7 keV are only a few times greater than the temperatures of 10–30 MK (or approximately 1–3 keV) that we obtain in the DEM calculation, suggesting that a warm-target model may be most appropriate. We can make direct comparisons with results for some of the flares that we have analyzed with results shown by Aschwanden et al. (2016), albeit for different time intervals. For example, in that work, the 2011 February 13 flare that we have been using for demonstration is shown to have a “warm-target” cutoff of 8.3 keV. This is close the limits that we obtain here, using a vastly different calculation and more assumptions. Most of the flares in the Aschwanden et al. (2016) have low (<10 keV) cutoff energies for the “warm-target” approximation.

Another consequence of the relatively low E_c values may affect the inferred dynamics of heating the thermal plasma in flares, in particular for the chromospheric evaporation process (Fisher et al. 1985)—it has been shown by Reep et al. (2015) that low-energy electrons are relatively more efficient at causing “explosive” evaporation.

As noted above, the original DEM model discussed by Caspi et al. (2014b) separately fit the Fe and Fe-Ni line complexes (at ~ 6.7 and ~ 8 keV), and did not use the CHIANTI package for those lines. This stemmed from suggestions by Phillips et al. (2006) and Caspi & Lin (2010) that the ionization fraction versus temperature for the Fe line complex may not be quite correct, based on analysis of *RHESSI* results. For this work, however, it is absolutely necessary to include the Fe line emission as modeled by the CHIANTI package, rather than fitting it separately, since tying the lines and continuum together provides the ability to constrain the high- T emission measure and subsequent thermal continuum emission model. We use the default CHIANTI ionization fraction model, as implemented in CHIANTI version 7.1.3 (Landi et al. 2013).

For most of the flares in the sample, we were able to attempt the calculation for both of the first two one-minute intervals during the start of flare. This added an extra level of validation in those cases; if the limits on E_c are not at least similar for the two time intervals in the same flare, and/or there is no systematic difference between the other model parameters for the two intervals, then we might suspect our calculations. Note that each calculation is independent for each interval; we do not use the common practice of relating the initial conditions for a subsequent time interval to those from the previous time interval in a given flare. For coronal abundances, for all 15 flares for which good limits were obtained for both intervals, the limits overlap. For photospheric abundances, only two flares yielded limits that did not overlap for their two intervals. This suggests that E_c may be relatively stable on the scale of minutes, but in the absence of good limits over the entire evolutions of multiple flare impulsive phases, we hesitate to draw a general conclusion.

It is important to note that, since we are looking at time intervals early during flares, the Fe XXV ions mostly responsible for the ~ 6.7 keV line complex may not be in equilibrium. The equilibrium time scale is dependent on the density of the hot plasma. Simple estimates for the high-temperature plasma density based on the size of the *RHESSI* image and the high- T emission measure (cf. Caspi 2010; Caspi et al. 2014b) give densities of order 10^{9-11} cm $^{-3}$, as shown in Table 2. Phillips (2004) suggested that for densities of 10^{10} cm $^{-3}$ or less, the ionization equilibrium may be problematic. However, we believe that ionization equilibrium is mostly attained since, for most of the flares, the ratios of counts and photon flux for the Fe line complex to the 10–12 keV continuum, $R(Fe)$ and $R_f(Fe)$, remain relatively stable from minute to minute during the flares for which we fit two intervals, as can be seen in Table 1. For 15 of 24 of these flares, the ratio $R_f(Fe)$ varies by less than 10%, and the variation is less than 25% for 18 of the 24. This would not be the case if the Fe XXV ionization had to “catch up” over time.

Table 2 shows the results for the flares for which we have two measurements, for high- T emission measure EM_{16} (the integral of the DEM for all $T > 16$ MK), volume V_{16} , density N_{16} , ionization time scale τ_{FeXXV} , and heating time scale τ_{HEAT} . The ionization time scale $\tau_{FeXXV} = 1/(N \times Q)$, where Q is the ionization rate for Fe XXIV to Fe XXV (Jordan 1970; Phillips 2004). The value of Q depends on temperature; for this case, since we are integrating over “all” high- T , we used an average of the values for $T = 10^{7.2-7.5}$, or $Q = 10^{-11.12}$. The heating time scale is given by $\tau_{HEAT} = ((1/EM_{16}) \times \delta(EM_{16})/\delta t)^{-1}$.

For all flares but one, τ_{FeXXV} is less (usually much less) than τ_{HEAT} . The one notable exception, 2012 November 14, exhibits a very low density value of $10^{8.9}$ cm $^{-3}$; the ratio $R_f(Fe)$

more than doubles between the two time intervals, suggesting that this case may indeed be affected by non-equilibrium ionization.

The calculation that we have done here for E_c is as comprehensive as we can get considering the available instrumentation. For future work it would be useful to have good observations of high- T line emissions that can be separated from the need to account for the non-thermal continuum, so that the entire thermal X-ray continuum can be estimated independently and subtracted, yielding the non-thermal component directly. The *Yohkoh* Bragg Crystal Spectrometer, with Ca XIX, Fe XXV, and Fe XXVI channels, is a good example of one such instrument useful for DEM analysis (Culhane et al. 1991; McTiernan et al. 1999). Soft X-ray spectra from, e.g., the *Miniature X-ray Solar Spectrometer*

(*MinXSS*; Mason et al. 2016; Moore et al. 2018) CubeSat, can provide additional diagnostics of the DEM and abundances for a number of elements (e.g., Caspi et al. 2015b; Woods et al. 2017). Combining *MinXSS* data with that from other instruments, particularly *RHESSI*, will open new areas of parameter space to further constrain E_c in different ways.

This work was funded by NASA Heliophysics Guest Investigator grants NNX12AH48G and NNX15AK26G. AC was also partially supported by NASA grants NNX14AH54G and NNX15AQ68G; JMM was partially supported by the *RHESSI* project, NASA grant NAS5-98033. All thermal emission is modeled using the CHIANTI software package (Dere et al. 1997; Landi et al. 2013).

REFERENCES

- Aschwanden, M. J., Holman, G., O’Flannagain, A., et al. 2016, *ApJ*, 832, 27, doi: [10.3847/0004-637X/832/1/27](https://doi.org/10.3847/0004-637X/832/1/27)
- Benz, A. O. 2017, *Living Reviews in Solar Physics*, 14, 2, doi: [10.1007/s41116-016-0004-3](https://doi.org/10.1007/s41116-016-0004-3)
- Brown, J. C. 1971, *SoPh*, 18, 489, doi: [10.1007/BF00149070](https://doi.org/10.1007/BF00149070)
- Caspi, A. 2010, PhD thesis, Department of Physics, University of California, Berkeley, CA 94720-7450, USA
- Caspi, A., Krucker, S., & Lin, R. P. 2014a, *ApJ*, 781, 43, doi: [10.1088/0004-637X/781/1/43](https://doi.org/10.1088/0004-637X/781/1/43)
- Caspi, A., & Lin, R. P. 2010, *ApJL*, 725, L161, doi: [10.1088/2041-8205/725/2/L161](https://doi.org/10.1088/2041-8205/725/2/L161)
- Caspi, A., McTiernan, J. M., & Warren, H. P. 2014b, *ApJL*, 788, L31, doi: [10.1088/2041-8205/788/2/L31](https://doi.org/10.1088/2041-8205/788/2/L31)
- Caspi, A., Shih, A. Y., McTiernan, J. M., & Krucker, S. 2015a, *ApJL*, 811, L1, doi: [10.1088/2041-8205/811/1/L1](https://doi.org/10.1088/2041-8205/811/1/L1)
- Caspi, A., Woods, T. N., & Warren, H. P. 2015b, *ApJL*, 802, L2, doi: [10.1088/2041-8205/802/1/L2](https://doi.org/10.1088/2041-8205/802/1/L2)
- Culhane, J. L., Hiei, E., Doschek, G. A., et al. 1991, *SoPh*, 136, 89, doi: [10.1007/BF00151696](https://doi.org/10.1007/BF00151696)
- Dennis, B. R., Phillips, K. J. H., Schwartz, R. A., et al. 2015, *ApJ*, 803, 67, doi: [10.1088/0004-637X/803/2/67](https://doi.org/10.1088/0004-637X/803/2/67)
- Dere, K. P., Landi, E., Mason, H. E., Monsignori Fossi, B. C., & Young, P. R. 1997, *A&AS*, 125, 149, doi: [10.1051/aas:1997368](https://doi.org/10.1051/aas:1997368)
- Donnelly, R. F., Grubb, R. N., & Cowley, F. C. 1977, NASA STI/Recon Technical Report N, 78
- Doschek, G. A., & Warren, H. P. 2017, *ApJ*, 844, 52, doi: [10.3847/1538-4357/aa7bea](https://doi.org/10.3847/1538-4357/aa7bea)
- Fisher, G. H., Canfield, R. C., & McClymont, A. N. 1985, *ApJ*, 289, 425, doi: [10.1086/162902](https://doi.org/10.1086/162902)
- Freeland, S. L., & Handy, B. N. 1998, *SoPh*, 182, 497, doi: [10.1023/A:1005038224881](https://doi.org/10.1023/A:1005038224881)
- Haug, E. 1997, *A&A*, 326, 417
- Jordan, C. 1970, *MNRAS*, 148, 17, doi: [10.1093/mnras/148.1.17](https://doi.org/10.1093/mnras/148.1.17)
- Kane, S. R., McTiernan, J., Loran, J., et al. 1992, *ApJ*, 390, 687, doi: [10.1086/171320](https://doi.org/10.1086/171320)
- Koch, H. W., & Motz, J. W. 1959, *Reviews of Modern Physics*, 31, 920, doi: [10.1103/RevModPhys.31.920](https://doi.org/10.1103/RevModPhys.31.920)
- Kontar, E. P., Jeffrey, N. L. S., Emslie, A. G., & Bian, N. H. 2015, *ApJ*, 809, 35, doi: [10.1088/0004-637X/809/1/35](https://doi.org/10.1088/0004-637X/809/1/35)
- Landi, E., Young, P. R., Dere, K. P., Del Zanna, G., & Mason, H. E. 2013, *ApJ*, 763, 86, doi: [10.1088/0004-637X/763/2/86](https://doi.org/10.1088/0004-637X/763/2/86)
- Leach, J., & Petrosian, V. 1981, *ApJ*, 251, 781, doi: [10.1086/159521](https://doi.org/10.1086/159521)
- Lin, R. P., Dennis, B. R., Hurford, G. J., et al. 2002, *SoPh*, 210, 3, doi: [10.1023/A:1022428818870](https://doi.org/10.1023/A:1022428818870)
- Longcope, D. W., & Guidoni, S. E. 2011, *ApJ*, 740, 73, doi: [10.1088/0004-637X/740/2/73](https://doi.org/10.1088/0004-637X/740/2/73)
- Mason, J. P., Woods, T. N., Caspi, A., et al. 2016, *Journal of Spacecraft and Rockets*, 53, 328, doi: [10.2514/1.A33351](https://doi.org/10.2514/1.A33351)
- McTiernan, J. M. 2009, *ApJ*, 697, 94, doi: [10.1088/0004-637X/697/1/94](https://doi.org/10.1088/0004-637X/697/1/94)
- McTiernan, J. M., Fisher, G. H., & Li, P. 1999, *ApJ*, 514, 472, doi: [10.1086/306924](https://doi.org/10.1086/306924)
- McTiernan, J. M., & Petrosian, V. 1990, *ApJ*, 359, 524, doi: [10.1086/169084](https://doi.org/10.1086/169084)
- Moore, C. S., Caspi, A., Woods, T. N., et al. 2018, *SoPh*, 293, 21, doi: [10.1007/s11207-018-1243-3](https://doi.org/10.1007/s11207-018-1243-3)
- Neupert, W. M. 1968, *ApJL*, 153, L59, doi: [10.1086/180220](https://doi.org/10.1086/180220)
- Pesnell, W. D., Thompson, B. J., & Chamberlin, P. C. 2012, *SoPh*, 275, 3, doi: [10.1007/s11207-011-9841-3](https://doi.org/10.1007/s11207-011-9841-3)
- Phillips, K. J. H. 2004, *ApJ*, 605, 921, doi: [10.1086/382523](https://doi.org/10.1086/382523)
- Phillips, K. J. H., Chifor, C., & Dennis, B. R. 2006, *ApJ*, 647, 1480, doi: [10.1086/505518](https://doi.org/10.1086/505518)
- Press, W. H., Teukolsky, S. A., Vetterling, W. T., & Flannery, B. P. 1992, *Numerical recipes in FORTRAN. The art of scientific computing*

- Reep, J. W., Bradshaw, S. J., & Alexander, D. 2015, *ApJ*, 808, 177,
doi: [10.1088/0004-637X/808/2/177](https://doi.org/10.1088/0004-637X/808/2/177)
- Saint-Hilaire, P., & Benz, A. O. 2005, *A&A*, 435, 743,
doi: [10.1051/0004-6361:20041918](https://doi.org/10.1051/0004-6361:20041918)
- Shibata, K. 1996, *Advances in Space Research*, 17, 9,
doi: [10.1016/0273-1177\(95\)00534-L](https://doi.org/10.1016/0273-1177(95)00534-L)
- Smith, D. M., Lin, R. P., Turin, P., et al. 2002, *SoPh*, 210, 33,
doi: [10.1023/A:1022400716414](https://doi.org/10.1023/A:1022400716414)
- Sui, L., Holman, G. D., & Dennis, B. R. 2007, *ApJ*, 670, 862,
doi: [10.1086/522198](https://doi.org/10.1086/522198)
- Warmuth, A., Holman, G. D., Dennis, B. R., et al. 2009, *ApJ*, 699,
917, doi: [10.1088/0004-637X/699/1/917](https://doi.org/10.1088/0004-637X/699/1/917)
- Warmuth, A., & Mann, G. 2016, *A&A*, 588, A115,
doi: [10.1051/0004-6361/201527474](https://doi.org/10.1051/0004-6361/201527474)
- Warren, H. P. 2014, *ApJL*, 786, L2,
doi: [10.1088/2041-8205/786/1/L2](https://doi.org/10.1088/2041-8205/786/1/L2)
- Warren, H. P., Mariska, J. T., & Doschek, G. A. 2013, *ApJ*, 770,
116, doi: [10.1088/0004-637X/770/2/116](https://doi.org/10.1088/0004-637X/770/2/116)
- Woods, T. N., Eparvier, F. G., Hock, R., et al. 2012, *SoPh*, 275,
115, doi: [10.1007/s11207-009-9487-6](https://doi.org/10.1007/s11207-009-9487-6)
- Woods, T. N., Caspi, A., Chamberlin, P. C., et al. 2017, *ApJ*, 835,
122, doi: [10.3847/1538-4357/835/2/122](https://doi.org/10.3847/1538-4357/835/2/122)
- Zharkova, V. V., Brown, J. C., & Syniavskii, D. V. 1995, *A&A*,
304, 284

Time tag	$E_c(\text{coronal})$	$E_c(\text{photo})$	$\text{Log}(\mathcal{E}_i)$ coronal	$\text{Log}(\mathcal{E}_i)$ photo	$\text{Log}(\mathcal{E}_{diff})$	χ^2 coronal	χ^2 photo	$R(Fe)$	$R_f(Fe)$
20110213_173136	5.0–10.4	6.6–10.1	28.4–29.8	28.7–29.3	1.1	0.82	1.06	0.62	17.08
20110213_173236	5.0–8.0	6.6–9.2	29.8–30.9	29.4–29.9	1.7	0.72	0.76	0.61	16.90
20110215_014812	5.0–9.1	5.1–9.6	29.7–31.0	29.5–30.4	1.6	0.65	0.70	0.51	13.26
20110215_014912	5.0–9.1	7.0–9.2	29.8–30.9	30.0–30.5	1.0	0.79	0.77	0.52	12.72
20110216_142304	5.0–30.0	5.0–30.0	26.9–27.7	26.9–29.5	–0.1	0.75	0.81	0.96	23.62
20110216_142404	5.0–9.7	5.0–10.2	29.3–30.9	29.3–30.2	2.9	0.72	0.81	0.79	29.32
20110224_072704	6.6–10.1	8.5–10.3	27.8–28.6	27.6–27.9	1.2	1.22	1.62	NA	30.80
20110228_124644	5.0–11.3	8.9–11.6	28.7–29.9	28.8–29.2	0.9	0.51	0.65	0.47	13.58
20110228_124744	7.0–10.2	7.7–10.6	29.1–30.0	29.2–29.9	1.3	0.86	1.08	0.61	16.80
20110307_194720	5.0–13.5	5.0–12.3	27.9–29.9	28.4–29.9	0.7	0.52	0.60	0.60	18.96
20110307_194820	5.0–12.6	5.0–12.0	28.2–29.4	28.5–29.5	0.7	0.81	0.86	0.69	20.27
20110307_214644	5.0–30.0	6.2–12.3	26.8–30.6	28.4–29.5	–1.5	0.65	0.56	0.55	15.37
20110307_214744	6.7–9.0	7.6–9.3	29.5–30.4	29.5–30.1	1.5	0.78	0.81	0.64	19.02
20110308_022736	5.0–8.6	5.0–9.9	29.3–30.9	29.0–30.6	2.8	0.56	0.53	0.59	18.75
20110308_022836	5.0–7.5	5.0–9.1	30.6–31.4	29.9–30.9	2.3	0.87	0.84	0.62	20.62
20110308_181012	5.0–7.2	9.4–10.3	28.9–29.3	28.4–28.5	2.0	0.86	0.60	NA	12.20
20110308_181044	5.0–29.7	5.0–24.6	27.3–28.3	27.5–30.0	–0.4	0.78	0.77	0.49	13.32
20110309_135740	5.0–30.0	5.0–11.6	20.1–28.9	28.8–29.5	0.8	0.66	1.08	0.95	32.15
20110309_135840	5.0–30.0	5.0–11.0	23.3–30.0	28.9–29.3	1.3	0.76	1.15	0.95	33.78
20110309_231820	5.0–9.8	7.1–10.9	29.3–31.0	29.3–29.8	1.6	0.60	0.89	0.67	22.05
20110309_231920	5.0–25.0	5.0–10.6	28.3–31.6	29.5–30.4	1.9	0.80	0.87	0.63	17.73
20110314_194952	5.0–6.3	5.0–8.7	30.6–31.2	29.6–30.5	2.7	0.78	0.89	0.66	23.29
20110314_195108	5.0–30.0	13.2–15.3	27.7–28.0	29.4–29.6	–0.3	0.97	0.73	0.58	23.55
20110315_002040	7.9–10.3	8.7–10.0	28.1–28.6	28.1–28.4	1.0	1.83	2.05	NA	22.16
20110315_002104	5.0–9.0	6.8–9.6	29.1–30.8	29.1–29.8	1.9	0.75	0.76	0.71	23.58
20110422_043824	5.0–30.0	5.0–11.0	25.7–27.5	28.4–29.1	–0.9	0.76	0.74	0.95	35.87
20110422_043924	5.0–30.0	5.0–12.7	22.4–29.2	28.4–29.1	1.5	0.54	0.92	1.13	36.33
20110529_101236	5.0–30.0	5.9–12.6	16.3–27.9	28.4–28.9	0.2	0.98	1.74	1.01	36.53
20110607_062044	6.4–10.1	9.0–10.2	27.9–28.7	27.7–28.0	1.1	0.96	1.16	NA	20.23
20110607_062144	8.3–9.1	7.7–9.1	28.4–28.6	28.3–28.7	1.1	1.68	2.32	NA	19.33
20110730_020652	5.0–11.8	5.0–12.1	27.5–28.3	27.4–27.8	0.6	0.67	0.79	NA	11.07
20110730_020732	5.0–24.5	5.0–21.6	28.2–31.3	28.4–28.7	–0.1	2.03	1.12	0.84	30.34
20110803_033428	5.0–6.4	5.0–9.4	30.8–31.5	29.2–30.1	3.1	1.51	1.83	0.86	34.85
20110803_043016	5.0–11.2	5.0–30.0	27.1–28.1	26.4–27.4	1.2	0.88	0.98	NA	8.93

Time tag	$E_c(\text{coronal})$	$E_c(\text{photo})$	$\text{Log}(\mathcal{E}_t)$ coronal	$\text{Log}(\mathcal{E}_t)$ photo	$\text{Log}(\mathcal{E}_{diff})$	χ^2 coronal	χ^2 photo	$R(Fe)$	$R_f(Fe)$
20110809_080028	16.4–24.9	5.0–9.6	27.3–27.6	29.1–30.1	–1.0	1.62	1.01	1.10	43.16
20110906_013736	5.0–8.1	5.0–10.1	29.5–30.2	28.7–29.6	2.5	1.22	1.15	0.62	20.08
20110906_221556	5.0–22.0	5.0–6.3	27.6–31.1	30.2–31.0	–0.5	1.68	0.66	0.87	35.54
20110908_153616	8.0–10.2	5.0–10.6	28.0–28.5	27.7–28.3	1.3	0.43	1.25	NA	30.85
20110908_153656	5.0–30.0	5.0–30.0	26.4–26.8	26.1–27.5	–0.3	1.64	0.53	1.37	60.26
20110924_171944	5.0–6.4	5.0–10.6	30.2–30.9	28.8–29.8	2.8	1.36	0.91	0.72	26.89
20110924_172044	5.0–5.1	5.0–5.7	31.8–31.8	31.5–31.9	3.0	2.23	2.08	0.60	24.71
20110924_191052	20.8–26.2	5.0–22.9	27.4–27.5	27.5–27.9	–1.0	2.66	1.52	0.97	47.35
20110924_203448	8.3–10.4	11.8–12.5	30.5–31.1	30.2–30.4	1.1	2.52	1.43	0.41	18.46
20110925_043448	5.0–5.4	5.0–14.7	31.2–31.5	28.1–28.6	3.6	2.56	2.77	0.90	41.07
20110926_050544	5.0–5.5	5.0–6.6	29.6–29.8	29.0–29.7	2.3	1.30	0.95	NA	5.06
20111002_004144	17.7–25.3	5.0–28.5	27.0–27.1	26.6–28.4	–0.4	1.95	1.22	1.07	53.14
20111105_030920	5.0–22.1	5.0–12.7	27.2–31.1	28.4–29.1	3.5	2.02	0.84	1.24	48.87
20111226_021836	5.0–30.0	5.0–30.0	25.7–25.9	25.4–27.0	–0.1	2.54	0.69	1.45	73.49
20111226_201544	17.7–26.4	5.0–21.8	27.2–27.4	27.4–27.8	–0.3	2.24	1.02	1.05	41.66
20111231_161908	5.0–10.2	8.9–11.1	27.9–28.9	27.7–28.0	0.8	0.87	0.82	NA	13.45
20121112_231852	5.0–9.3	8.0–10.4	29.0–30.1	28.8–29.6	1.6	0.77	1.29	0.67	26.80
20121112_231952	5.0–11.4	8.2–10.1	27.3–29.8	28.6–29.1	1.3	2.29	2.71	0.88	41.99
20121113_054512	6.7–7.0	6.8–8.0	29.2–29.3	28.8–29.2	1.9	0.79	0.85	NA	15.00
20121113_054556	5.0–7.0	5.0–7.8	30.2–31.1	29.8–31.1	2.9	0.99	0.78	0.70	27.16
20121114_040052	5.0–10.1	5.0–10.2	27.3–28.6	27.3–28.6	1.3	0.55	0.55	NA	5.26
20121114_040152	6.6–7.0	6.8–7.3	28.9–29.0	28.7–28.9	1.7	1.21	1.15	NA	12.51
20121120_123808	5.5–6.0	7.0–8.1	29.6–29.9	28.8–29.2	2.3	2.76	2.34	NA	24.11
20121120_123844	5.0–8.0	6.9–8.3	29.8–31.1	29.7–30.3	1.9	0.88	0.78	0.74	24.27
20121121_064900	5.0–8.6	6.5–9.5	29.3–30.7	29.1–29.9	1.8	0.62	0.67	0.57	18.36
20121128_213200	6.4–8.0	8.5–9.2	30.1–30.8	29.8–30.0	2.0	0.85	1.11	0.72	26.22
20121128_213300	6.6–8.2	8.8–9.1	30.2–30.8	30.0–30.1	2.0	1.14	1.37	0.76	27.60
20130111_085900	5.0–30.0	12.6–14.2	25.0–28.3	28.2–28.4	0.7	0.51	1.00	0.75	26.00
20130113_004744	5.0–14.0	5.0–13.1	27.2–27.7	27.1–27.8	0.3	0.70	0.70	NA	6.05
20130113_004840	5.0–9.3	7.8–9.7	29.1–30.7	29.3–29.9	1.6	0.83	1.13	0.78	25.29
20130217_154632	6.8–8.2	7.8–9.0	28.6–29.1	28.4–28.7	1.6	2.47	2.44	NA	36.00
20130217_154704	5.0–9.3	9.5–12.7	28.8–30.7	28.6–29.1	2.8	0.65	0.81	0.88	32.58

Table 1. Fitting results. Values (columns) for each time interval (row) are: interval date and time; derived limits for E_c using coronal and photospheric abundances; derived limits for \mathcal{E}_t (total electron energy) for coronal and photospheric abundances; minimum (best-fit) values of *reduced* χ^2 using coronal and photospheric abundances; difference between \mathcal{E}_t values for the derived E_c and $E_c = 15$ keV; $R(Fe)$, the ratio of the count rate in the ~ 6.7 keV Fe line complex to the peak of the count rate in the 10–20 keV range; and $R_f(Fe)$, the ratio of the fitted photon flux in the Fe line complex to the photon flux in the 10–20 keV range. For $R(Fe)$, “NA” means that there was no separate peak in the count spectrum, due to the fact that the thin attenuator was out.

Time tag	$\text{Log}(EM_{16})$ (cm^{-3})	$\text{Log}(N_{16})$ (cm^{-3})	$\text{Log}(V_{16})$ (cm^3)	τ_{FeXXV} (s)	τ_{HEAT} (s)
20110213_173136,173236	46.9	9.8	27.3	19.	43.
20110215_014812,014912	47.9	10.4	27.2	6.	81.
20110216_142304,142404	47.4	10.3	26.7	7.	87.
20110228_124644,124744	46.9	10.0	26.8	12.	61.
20110307_194720,194820	46.4	9.8	26.8	20.	233.
20110307_214644,214744	47.1	10.2	26.6	8.	39.
20110308_022736,022836	47.6	10.6	26.3	3.	52.
20110308_181012,181044	46.9	10.0	26.9	13.	35.
20110309_135740,135840	47.0	9.7	27.7	27.	213.
20110309_231820,231920	48.1	10.7	26.7	3.	76.
20110314_194952,195108	48.7	11.0	26.6	1.	34.
20110315_002040,002104	47.2	10.1	27.0	11.	34.
20110422_043824,043924	47.0	10.3	26.4	7.	54.
20110607_062044,062144	46.1	9.4	27.3	47.	56.
20110730_020652,020732	47.9	10.6	26.7	3.	30.
20110908_153616,153656	46.8	10.0	26.8	12.	34.
20110924_171944,172044	47.4	10.5	26.5	5.	42.
20121112_231852,231952	46.8	10.1	26.6	11.	77.
20121113_054512,054556	47.0	9.9	27.2	17.	31.
20121114_040052,040152	45.1	8.9	27.2	151.	39.
20121120_123808,123844	47.3	9.9	27.4	15.	30.
20121128_213200,213300	47.9	10.7	26.5	2.	83.
20130113_004744,004840	47.4	10.1	27.1	9.	30.
20130217_154632,154704	47.4	10.3	26.8	7.	31.

Table 2. Results for evaluating ionization equilibrium for flares where two consecutive time intervals could be fit, using volume estimates from *RHESSI* images. For each flare (row), values (columns) are: EM_{16} , the total emission measure for plasma with $T > 16$ MK ($\text{Log}(T) > 7.2$), integrated from the DEM; N_{16} , the plasma density; V_{16} , the volume estimated from *RHESSI* images; τ_{FeXXV} , the time scale for ionization equilibrium of Fe XXV; and τ_{HEAT} , the heating time scale.